JOURNAL OF AIRCRAFT
Vol. 45, No. 6, November–December 2008

Bioinspired Corrugated Airfoil at Low Reynolds Numbers

Hui Hu* and Masatoshi Tamai†
Iowa State University, Ames, Iowa 50011

DOI: 10.2514/1.37173

An experimental study was conducted to investigate the flow behavior around a bioinspired corrugated airfoil compared with a traditional streamlined airfoil and a flat plate at the chord Reynolds number of $Re = 34,000$ to explore the potential application of such bioinspired corrugated airfoils for micro air vehicle applications. The experiments were conducted in a low-speed wind tunnel. A high-resolution particle image velocimetry system was used to conduct detailed flowfield measurements to quantify the transient behavior of vortex and turbulent flow structures around the studied airfoils. The particle image velocimetry measurement results demonstrated clearly that the corrugated airfoil has better performance over the streamlined airfoil and the flat plate in preventing large-scale flow separation and airfoil stall at low Reynolds numbers. It was found that the protruding corners of the corrugated airfoil would act as turbulators to generate unsteady vortex structures to promote the transition of the separated boundary-layer flow from laminar to turbulent. The unsteady vortex structures trapped in the valleys of the corrugated cross section would pump high-speed fluid from outside to near-wall regions to provide sufficient kinetic energy for the boundary layer to overcome adverse pressure gradients, thus discouraging large-scale flow separations and airfoil stall. Aerodynamic force measurements further confirmed the possibility of using such bioinspired corrugated airfoils in micro air vehicle designs to improve their flight agility and maneuverability.

Introduction

MICRO air vehicles (MAVs) with a wingspan of 15 cm or shorter and a flight speed of around 10 m/s have attracted substantial interest in recent years. Although a number of MAVs, either in fixed-wing or flapping-wing designs, have already been developed by several universities and commercial- and government-funded endeavors, the airfoil and wing planform designs of the MAVs rely mainly on scaled-down versions of those used by conventional macroscale aircraft. Chord Reynolds number Re, which is based on airfoil chord length and flight velocity, is used to characterize the aerodynamic performance of an airfoil. Whereas traditional macroscale aircraft have a chord Reynolds number of about 10^6–10^8, the chord Reynolds numbers of MAVs are usually in the range of 10^4–10^5. The aerodynamic design principles applicable to traditional macroscale aircraft may not be used for MAVs, due to the significant difference in chord Reynolds numbers. As a result, airfoil shape and wing planform designs that are optimized for traditional macroscale aircraft are found to degrade significantly when used for MAVs [1]. Therefore, it is very necessary and important to establish novel airfoil shape and wing planform design paradigms for MAVs to achieve good aerodynamic performance as well as flight agility and versatility.

A number of insects, including locusts, dragonflies, and damselflies, employ wings that are not smooth or simple cambered surfaces. The cross sections of the wings have well-defined corrugated configurations [2,3]. Such corrugated design was found to be of great importance to the stability of the ultralight wings to handle the spanwise bending forces and mechanical wear that the wing experiences during flapping. The corrugated wing design does not appear to be very suitable for flight because it would have very poor aerodynamic performance (i.e., low lift and extremely high drag) according to traditional airfoil design principles. However, several studies on corrugated dragonfly wings in steady flow or gliding flight [4–17] have led to a surprising conclusion: a corrugated dragonfly wing could have comparable or even better aerodynamic performances (i.e., higher lift and bigger lift-to-drag ratio) than conventional streamlined airfoils in the low Reynolds number regime in which dragonflies usually fly.

Most of the earlier experimental studies were conducted mainly based on the measurements of total aerodynamic forces (lift and drag) of either natural dragonfly wings or modeled corrugated wing sections. Detailed studies were conducted more recently to try to elucidate the fundamental physics of the dragonfly flight aerodynamics [12–17]. A number of hypotheses have been suggested to explain the fundamental mechanism of the rather unexpected aerodynamic performance improvement of the corrugated dragonfly airfoils or wings over conventional smooth airfoils. Rees [4] suggested that airflow could be trapped in the valleys of the corrugated structures to become stagnant or rotate slowly in the valleys, resulting in the corrugated wing acting as a streamlined airfoil. Newman et al. [5] suggested that the improved aerodynamic performance would be associated with the earlier reattachment of the flow separation on the corrugated wings. As the angle of attack increases, airflow would separate from the leading edge to form a separation bubble, and the separated flow would reattach sooner due to the corrugation, compared with smooth airfoils. Based on pressure measurements on the surfaces of a dragonfly wing model in addition to total lift-and-drag force measurements, Kesel [12] reported that negative pressure would be produced at the valleys of the corrugated dragonfly wing model, which would contribute to the increased lift. Vargas and Mittal [15] and Luo and Sun [16] conducted numerical studies to investigate the flow behaviors around corrugated dragonfly wings. Their simulation results confirmed the existence of small vortex structures in the valleys of the corrugated dragonfly airfoil. The small vortex structures in the valleys of the corrugated cross section were also revealed qualitatively in the flow-visualization experiments of Kwok and Mittal [17].

Despite different explanations about the fundamental mechanism for the improved aerodynamic performance, most of the studies agree that corrugated dragonfly airfoils or wings work well in low Reynolds number regimes, which naturally point to the potential applications of employing such corrugated airfoils or wings in micro

Received 16 February 2008; revision received 1 May 2008; accepted for publication 3 May 2008.

*Assistant Professor, Aerospace Engineering Department; huhui@iastate.edu. Senior Member AIAA.
†Graduate Student, Aerospace Engineering Department.

air vehicles. With this in mind, we conducted the present study to try to leverage the corrugation feature of dragonfly wings and to explore the potential applications of such nontraditional bioinspired corrugated airfoils to MAV designs for improved aerodynamic performance.

Although several experimental studies have already been conducted previously to investigate the aerodynamic performance of corrugated dragonfly airfoils or wings, detailed quantitative flow measurements have never been made to elucidate the underlying physics of why and how corrugated airfoils or wings could have comparable or even better aerodynamic performance for low Reynolds number flight. It should also be noted that the majority of previous studies on dragonfly wings or modeled dragonfly airfoils were conducted from a biologist's point of view to try to understand the fundamental mechanism of dragonfly flight mechanics; thus, the chord Reynolds number level of those studies is usually relatively small (i.e., $Re \leq 10,000$). In the present study, we report a detailed experimental investigation to quantify the flow behavior around a bioinspired corrugated airfoil, compared with a conventional streamlined airfoil and a flat plate at low Reynolds numbers. The experimental study was conducted in a wind tunnel with particle image velocimetry (PIV) to make detailed flowfield measurements in addition to total aerodynamic force (drag-and-lift) measurements. It should be noted that the present study was conducted with a fixed 2-D corrugated-airfoil model in steady flows, whereas dragonflies fly with flapping corrugated wings. As described by Newman et al. [5], because the average flapping frequency of dragonfly flight is roughly 25 Hz with a forward flight speed of $\sim$10 m/s, so that in one cycle of wing flapping, a dragonfly would move forward about 40 chord lengths. It is therefore postulated that aerodynamics may be usefully studied, at least initially, on a static wing in a steady flow. The present study is conducted from the viewpoint of an aerospace engineer to explore the potential applications of such nontraditional bioinspired corrugated airfoils in MAV designs. Thus, we chose to conduct the present study at the chord Reynolds number of $Re = 34,000$ (i.e., in the range in which MAVs usually operate), which is much higher than those previous experiments to study dragonfly flight aerodynamics.

Experimental Setup and Studied Airfoils

The experimental study was conducted in a closed-circuit low-speed wind tunnel located in the Aerospace Engineering Department of Iowa State University. The tunnel has a test section with a 1.0×1.0 ft (30×30 cm) cross section, and the walls of the test section are optically transparent. The tunnel has a contraction section upstream of the test section with honeycombs, screen structures, and a cooling system installed ahead of the contraction section to provide uniform low turbulent incoming flow into the test section.

Figure 1 depicts the three airfoils used in the present study: a streamlined airfoil GA (W)-1 [also labeled as NASA LS(1)-0417] airfoil, a flat-plate airfoil, and a bioinspired corrugated airfoil.

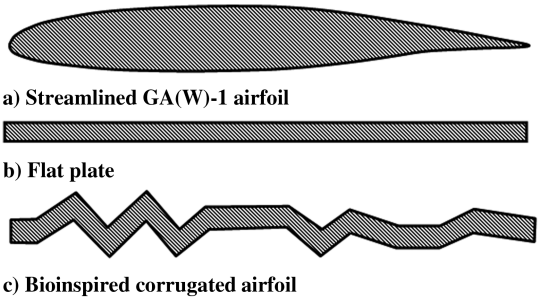

Fig. 1 The test airfoils.

Compared with standard NACA airfoils, the GA (W)-1 airfoil was specially designed for low-speed aviation applications with a large leading-edge radius to flatten the peak in the pressure-coefficient profile near the airfoil nose to discourage flow separation [18]. The GA (W)-1 airfoil has a maximum thickness of 17% of the chord length. The flat plate has a rectangular cross section. The cross section of the bioinspired corrugated airfoil corresponds to a typical cross section of a dragonfly wing, which was digitally extracted from the profile given in Vargas and Mittal [15]. The flat plate and the bioinspired corrugated airfoil are made of wood plates with a thickness of 4.0 mm. The maximum effective thickness of the corrugated airfoil (i.e., the airfoil shape formed by fitting a spline through the protruding corners of the corrugated cross section) is about 15% of the chord length, which is slightly smaller than that of the streamlined GA(W)-1 airfoil (17% of the chord length). The flat-plate airfoil, bioinspired corrugated airfoil, and streamlined GA (W)-1 airfoil have the same chord length: that is, $C = 101$ mm. The flow velocity at the inlet of the test section was set at $U_\infty = 5.0$ m/s for the present study, which corresponds to a chord Reynolds number of $Re = 3.4 \times 10^4$. The turbulence intensity of the incoming stream was found to be within 1.0%, measured by using a hot-wire anemometer.

Figure 2 shows the experimental setup used in the present study for PIV measurements. The test airfoils were installed in the middle of the test section. A PIV system was used to make flow-velocity field measurements along the chord at the middle span of the airfoils. The flow was seeded with 1–5-μm oil droplets. Illumination was provided by a double-pulsed Nd:YAG laser (NewWave Gemini 200) adjusted on the second harmonic and emitting two pulses of 200 mJ at the wavelength of 532 nm with a repetition rate of 10 Hz. The laser beam was shaped to a sheet by a set of mirrors and spherical and cylindrical lenses. The thickness of the laser sheet in the measurement region is about 0.5 mm. A high-resolution 12-bit (1376×1040 pixels) CCD camera (SensiCam-QE, Cooke Corp.) was used for PIV image acquisition, with the axis of the camera perpendicular to the laser sheet. The CCD cameras and the double-pulsed Nd:YAG lasers were connected to a workstation (host computer) via a digital delay generator (Berkeley Nucleonics, model

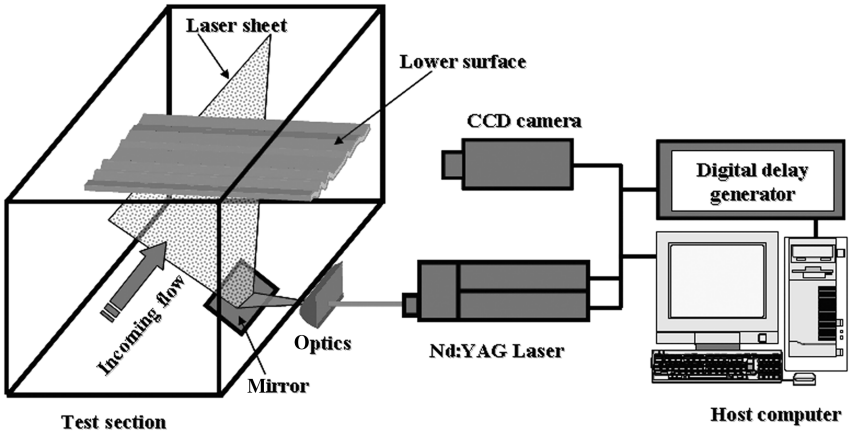

Fig. 2 Experimental set up for PIV measurements.

565), which controlled the timing of the laser illumination and image acquisition.

Instantaneous PIV velocity vectors were obtained by a frame-to-frame cross-correlation technique involving successive frames of patterns of particle images in an interrogation window of 32×32 pixels. An effective overlap of 50% of the interrogation windows was employed in PIV image processing. The PIV measurements were conducted at two spatial resolutions: a coarse level to study the global features of the flowfields around the airfoils, with a measurement window size of about 200×160 mm, and a finer level to investigate the detailed flow structures near the leading edges of the airfoils, with a measurement window size of about 50×40 mm. The effective resolutions of the PIV measurements (i.e., grid sizes) were $D/C = 0.048$ and 0.012, respectively. After the instantaneous velocity vectors u_i and v_i were determined, instantaneous spanwise vorticity ω_z could be derived. The time-averaged quantities such as mean velocity (U, V), ensemble-averaged spanwise vorticity, turbulent velocity fluctuations $(\bar{u}', \bar{v}')$, and normalized turbulent kinetic energy $[\mathrm{TKE} = (\bar{u}'^2 + \bar{v}'^2)/2U_\infty^2]$ distributions were obtained from a cinema sequence of 280 frames of instantaneous velocity fields. The measurement uncertainty level for the velocity vectors is estimated to be within 2.0% and that of the turbulent velocity fluctuations $(\bar{u}', \bar{v}')$ and TKE are about 5.0%. The aerodynamic forces (lift and drag) acting on the test airfoils were also measured by using a force-moment sensor cell (JR3, model 30E12A-I40). The force-moment sensor cell is composed of foil strain-gauge bridges, which are capable of measuring the forces on three orthogonal axes and the moment (torque) about each axis. The precision of the force-moment sensor cell for force measurements is $\pm 0.25\%$ of the full scale (40 N).

Experimental Results and Discussions

Figure 3 shows the measured ensemble-averaged velocity field and corresponding streamlines around the test airfoils at a 5.0-deg angle of attack. As shown in the results given in Fig. 3a, incoming fluid streams were found to flow smoothly along the streamlined nose of the GA(W)-1 airfoil, as expected. However, flow separation was found to take place near the trailing edge of the airfoil even at a 5.0-deg angle of attack because of the low Reynolds number. As a result of the flow separation, a large circulation region was found in the wake of the GA(W)-1 airfoil.

For the flat plate, as revealed clearly from the measurement results given in Fig. 3b, incoming fluid streams were found to separate from the surface of the flat plate right from the leading edge and then reattach to the upper surface of the flat plate in the near leading-edge portion of the flat plate; that is, a circulation bubble was found to form on the upper surface near the leading edge of the flat plate. Because of the reattachment of the separated fluid streams, no apparent flow separation or large circulation region could be found in the wake of the flat plate.

For the bioinspired corrugated airfoil, the existence of a circulation bubble near the leading edge of the airfoil can be seen clearly from the measurement results given in Fig. 3c at a 5.0-deg angle of attack. Smaller circulation bubbles (an enlarged view is given later) were found to sit in the valleys of the corrugated cross section. High-speed fluid streams outside the corrugation valleys were found to flow smoothly along a virtual envelope profile constructed by fitting a spline through the protruding corners of the corrugated cross section (i.e., a smooth shape formed by filling the small circulation bubbles solidly into the corrugation valleys). No apparent large-scale flow separation or circulation region could be found in the wake of the corrugated airfoil at a 5.0-deg angle of attack.

Figure 4 shows the PIV measurement results when the angle of attack of the airfoils increases to 10.0 deg. For the GA (W)-1 airfoil, the separation point at which high-speed flow streams begin to separate from the upper surface of the GA (W)-1 airfoil was found to move further upstream to approach the airfoil leading edge. Flow separation was found to take place on almost the entire upper surface of the airfoil; that is, the GA (W)-1 airfoil was found to stall, resulting in a very large circulation region in the wake of the airfoil. The large deficit of the velocity profile in the wake of the GA (W)-1 airfoil would indicate a rapid increase of the aerodynamic drag force acting on the airfoil due to the airfoil stall, which was confirmed from the drag force measurement data given in Fig. 10.

For the flat plate, the circulation bubble on the upper surface near the leading edge was found to burst when the angle of attack increased to 10.0 deg. The high-speed flow streams separated from the upper surface at the leading edge of the flat plate could no longer reattach to the upper surface of the flat plate. Large-scale flow separation was found to occur on entire upper surface of the flat plate (i.e., airfoil stall), due to a more severe adverse pressure gradient at a 10.0-deg angle of attack. However, for the corrugated airfoil, high-speed fluid streams were still found to faithfully follow the envelope profile of the corrugated cross section, and no large-scale flow separation could be found over the corrugated airfoil at a 10.0-deg angle of attack.

The adverse pressure gradient over the upper surface of the airfoils would become more and more severe as the angle of attack increased. Compared with those at a 10.0-deg angle of attack, the circulation regions in the wakes of the GA (W)-1 airfoil and the flat plate were found to be enlarged significantly when the angle of attack increased to 15.0 deg (Fig. 5a and 5b), which would indicate increased aerodynamic drag forces acting on the airfoils. Because of the severe adverse pressure gradient at a 15.0-deg angle of attack, high-speed flow streams around the corrugated airfoil were not able to follow the envelope profile of the corrugated cross section any longer. Large-scale flow separation was found to occur over almost the entire upper surface of the corrugated airfoil; that is, airfoil stall was also found for the bioinspired corrugated airfoil at a 15.0-deg angle of attack.

The PIV measurement results demonstrated clearly that the bioinspired corrugated airfoil could delay large-scale flow separation and airfoil stall to a much higher angle of attack (up to about 12.0 deg) compared with the streamlined GA-1(W) airfoil (airfoil stall at a 9.0-deg AOA) and the flat plate (airfoil stall at an 8.0-deg AOA). To elucidate the fundamental reason why corrugated airfoils have better performance in preventing large-scale flow separation and delaying airfoil stall compared with streamlined airfoils and flat plates at low Reynolds numbers, refined PIV measurements near the leading edges of the airfoils were made to investigate detailed flow structures around the leading edges of the airfoils. The refined PIV measurement results are given in Figs. 6–9.

As described in the review articles of Lissaman [19] and Gad-el-Hak [20] for streamlined airfoils at low Reynolds numbers, the boundary layers would remain laminar at the onset of the pressure recovery unless artificially tripped. Laminar boundary layers are unable to withstand any significant adverse pressure gradient. Therefore, the aerodynamic performances of traditional streamlined airfoils at low Reynolds numbers are entirely dictated by the relatively poor separation resistance of the laminar boundary layers. The laminar boundary layer over the streamlined GA (W)-1 airfoil was visualized clearly as a thin vortex layer over the nose of the airfoil in the instantaneous vorticity distribution given in Fig. 6. As indicated in the PIV measurement results, the laminar boundary layer would separate from the upper surface of the streamlined airfoil because the laminar boundary layer has a very poor capacity to overcome the adverse pressure gradient. Laminar flow separation would take place on the upper surface of the GA (W)-1. The separated laminar boundary layer would behave more like a free shear layer, which is highly unstable; therefore, rolling up of Kelvin–Helmohtz vortex structures and transition to turbulence would be readily realized. Because of the laminar nature of the flow around the nose of the streamlined airfoil, the regions with higher TKE were found to be confined within the thin separated shear layer.

Figure 7 reveals the flow behavior around the leading edge of the flat plate at a 10-deg angle of attack. Because of the low Reynolds number, incoming flow streams were found to separate from the leading edge of the flat plate to form a separated laminar shear layer. The laminar shear layer was found to transition to turbulence by generating unsteady Kelvin–Helmohtz vortex structures. Compared with those found near the nose of the streamlined GA (W)-1 airfoil, the Kelvin–Helmohtz vortex structures near the flat-plate leading

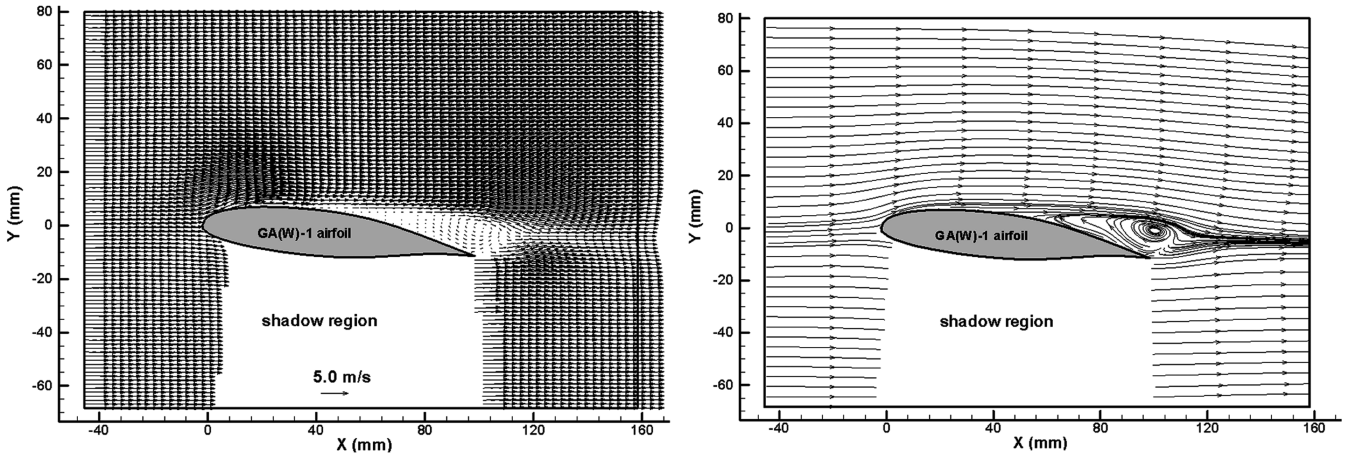

a) Streamlined airfoil

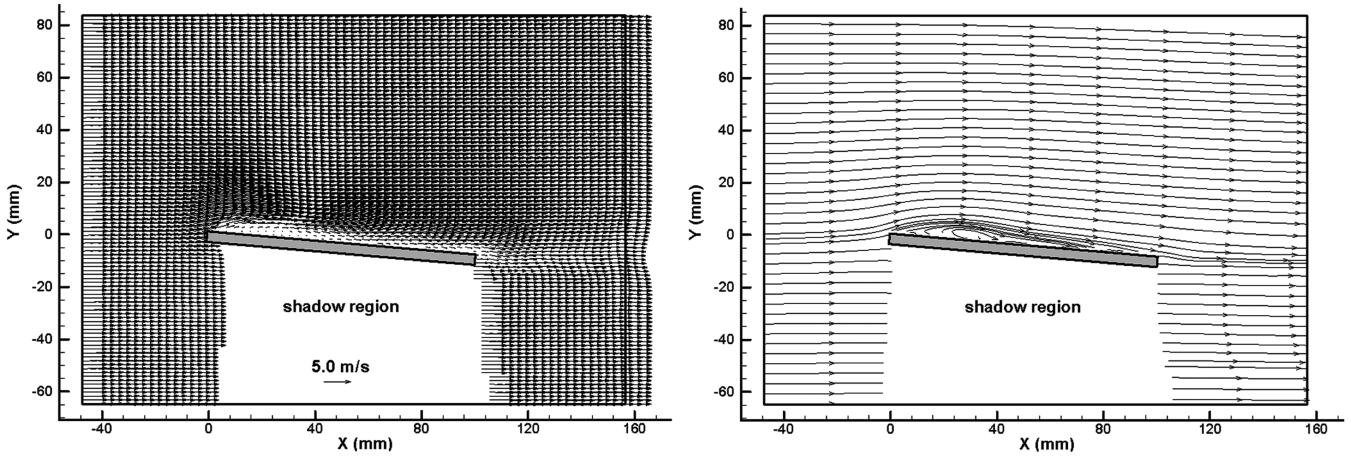

b) Flat plate

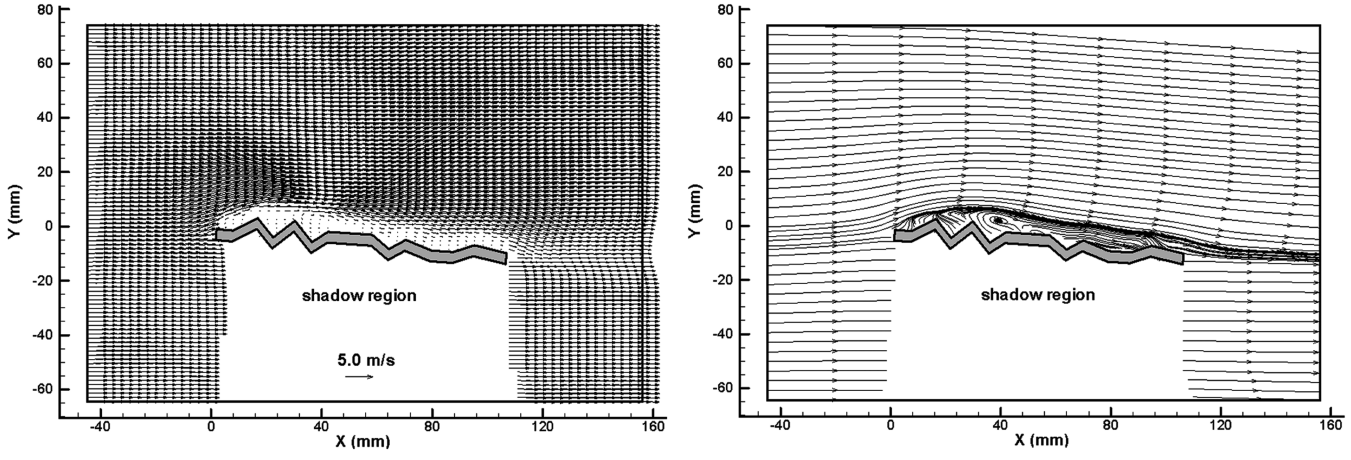

c) Bioinspired corrugated airfoil

Fig. 3 PIV measurement results at 5.0-deg AOA; ensemble-averaged velocity field (left) and corresponding streamlines (right).

edge were found to be much stronger, which results in a much higher turbulent kinetic energy level compared with that of the streamlined GA(W)-1 airfoil. As shown in Fig. 3, due to the sharp leading edge of the flat plate, incoming fluid streams would separate from the upper surface of the flat plate right from the shape leading edge. The separated fluid streams could reattach to the upper surface of the plate to form a circulation bubble on the upper surface of the flat plate when the advance pressure gradient on the upper surface of the flat plate is rather mild at relatively small angles of attack. However, when the angle of attack is relatively large (AOA $>$ 8.0) and the adverse pressure gradient over the upper surface of the flat plate becomes more significant, the separated fluid streams would no longer be able to reattach to the upper surface of the flat plate. The circulation bubble near the leading edge would then burst to cause airfoil stall, as shown in Fig. 4.

Flow around the leading edge of the corrugated airfoil is much more involved than those of the flat plate and the GA (W)-1 airfoil. As visualized in the PIV measurement results given in Fig. 8, due to the sharp leading edge, incoming fluid streams were found to separate from the corrugated airfoil right from the sharp leading edge to form a laminar shear layer at first. Then the separated laminar boundary layer was found to transition to turbulent rapidly as it approached the first protruding corner of the corrugated airfoil. Unsteady vortices were found to shed periodically from the protruding corners of the corrugated cross section; that is, the protruding corners of the corrugated airfoil seem to act as turbulators

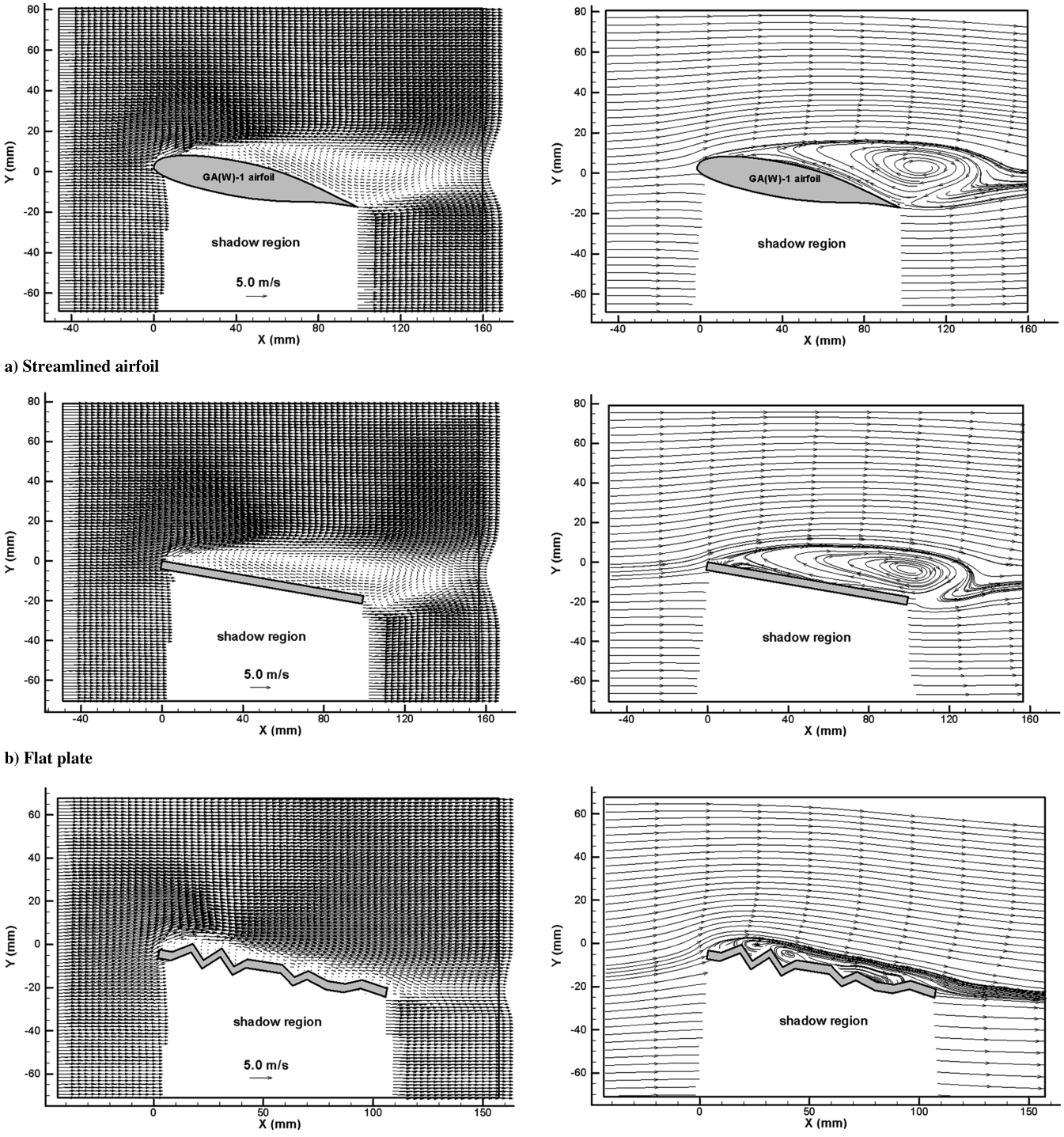

Fig. 4 PIV measurement results at a 10.0-deg AOA; ensemble-averaged velocity field (left) and corresponding streamlines (right).

to generate unsteady vortex structures that promote the transition of the separated boundary layer from laminar to turbulent. For the streamlined GA (W)-1 airfoil and flat plate at the same angle of attack of 10 deg, the turbulent transition and the generation of the unsteady vortex structures were found to take place in the regions relatively far away from the surfaces of the airfoils, as revealed in the measurement results given in Figs. 6 and 7. For the corrugated airfoil, the turbulent transition and the generation of the unsteady vortex structures were found to take place in the region quite close to the protruding corners of the corrugated airfoil. The unsteady vortex structures were found to be trapped in the valleys of the corrugated cross section, which would dynamically interact with the high-speed flow streams outside the valleys. Because of the interaction between the unsteady vortex structures and outside high-speed fluid streams, high-speed fluid was found to be pumped from outside to near-wall regions (the pumping effect of the unsteady vortex structures to move high-speed fluid from outside to near-wall regions can be seen clearly from the animations of the time sequence of instantaneous PIV measurements). The pumping of high-speed fluid to near-wall regions provided sufficient kinetic energy for the boundary layer to overcome the adverse pressure gradient to suppress large-scale flow separation and airfoil stall. The mean velocity vectors and corresponding streamlines revealed clearly that small circulation bubbles would be formed in the valleys of the corrugated airfoil. High-speed fluid streams outside the valleys would flow smoothly along the envelope profile of the corrugated cross section (i.e., the

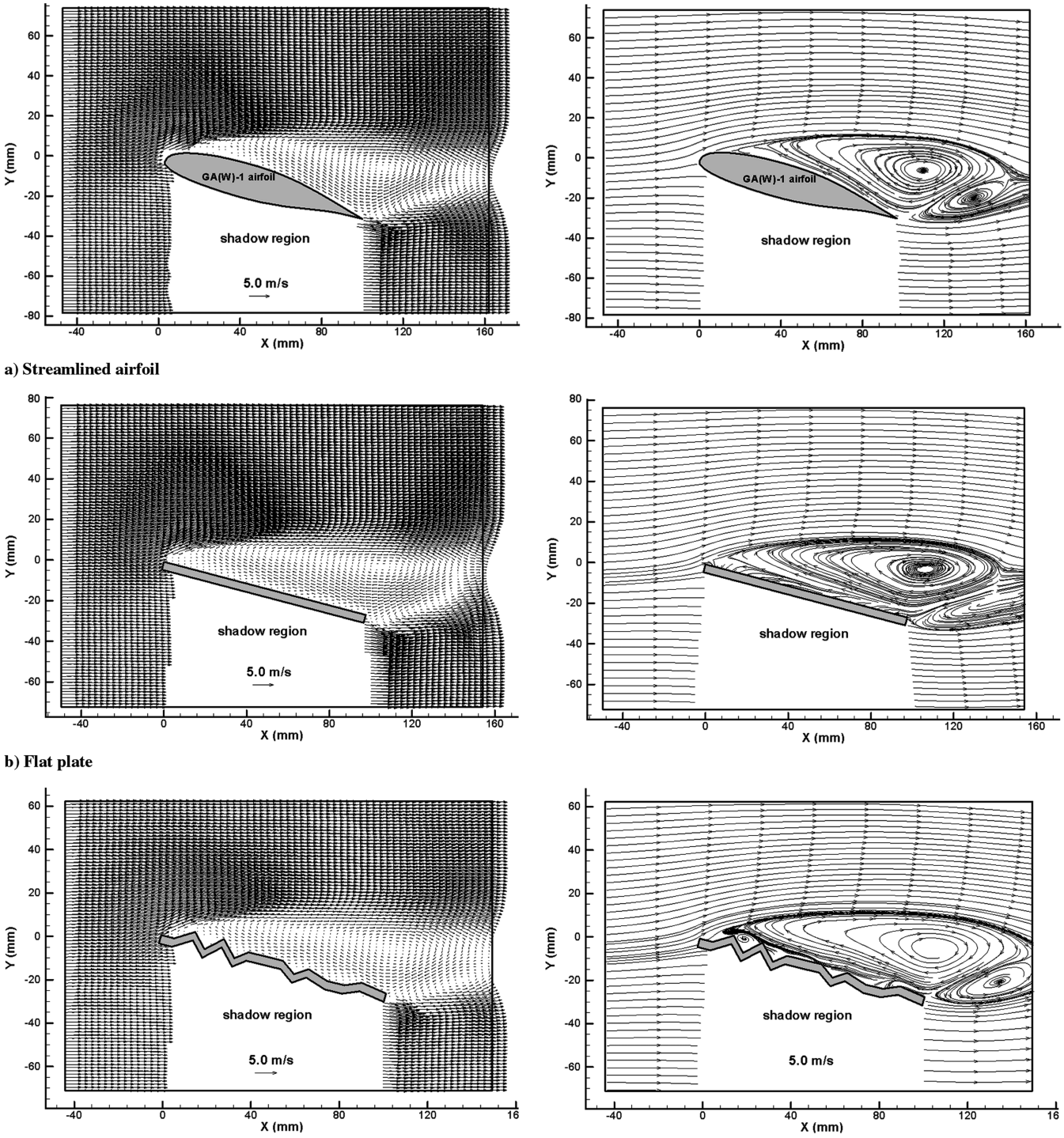

Fig. 5 PIV measurement results at a 15.0-deg AOA; ensemble-averaged velocity field (left) and corresponding streamlines (right).

profile was formed as the valleys were solidly filled with the small circulation bubbles). The rotation direction of the circulation bubbles in the valleys was found to be clockwise (flow moving from left to right) to accommodate the high-speed fluid streams outside the valleys. For the corrugated airfoil, the rapid transition of the boundary layer from laminar to turbulent due to the effect of the protruding corners as turbulators could also be seen clearly from the measured TKE distribution, in which the contour lines of the regions with higher turbulent kinetic energy were found to diverge rapidly after reaching the first protruding corner of the corrugate airfoil. The entrainment of high-speed fluid to near-wall regions by the unsteady vortex structures resulted in a much higher TKE level in the near-wall regions.

It should be noted that Vargas and Mittal [15] conducted a numerical study to investigate flow structures around a corrugated airfoil similar to that used in the present study, but at a lower Reynolds number level of $Re = 10,000$. Despite the difference in Reynolds number of the two studies, the measurement results of the present study were found to agree well with the numerical simulation of Vargas and Mittal in revealing the global pattern of the flowfield around the corrugated airfoil and the small vortex structures in the valleys of the corrugated cross section.

Compared with those of the streamlined GA (W)-1 airfoil and flat plate, the energetic turbulent boundary layer over the upper surface of the corrugated airfoil would be much more capable of advancing against an adverse pressure gradient, suppressing flow

separation [19,20]. Therefore, flow streams would be able to attach to the envelope profile of the corrugated airfoil faithfully even at much larger angles of attack (up to 12.0 deg), whereas the large-scale flow separation and airfoil stall had already been found to take place for the flat plate and the streamlined GA (W)-1 airfoil.

As shown in Fig. 9, although the separated laminar boundary layer was found still to transition to turbulence rapidly by generating

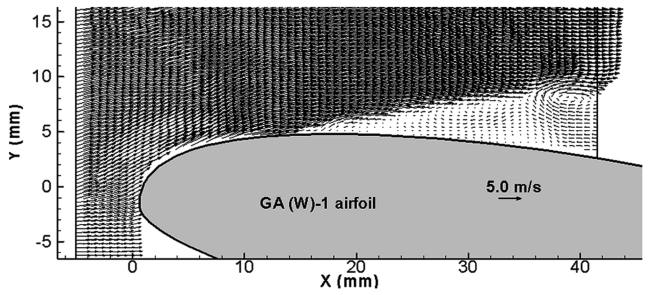

a) Instantaneous velocity field

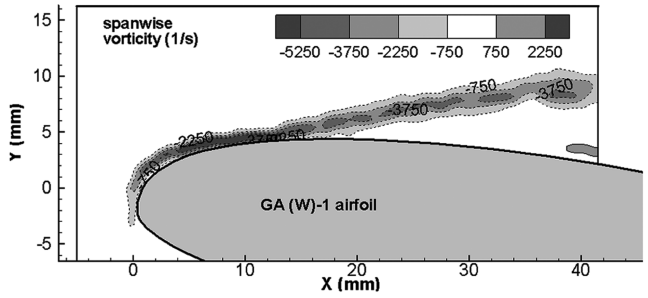

b) Instantaneous vorticity distribution

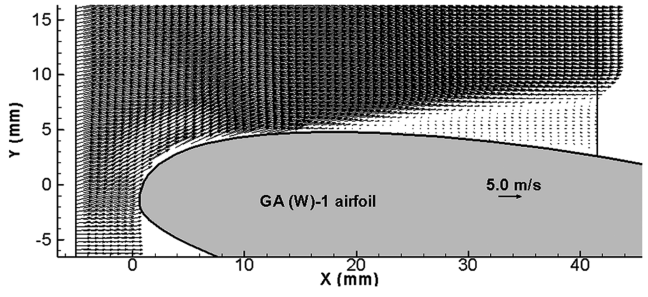

c) Ensemble-averaged velocity field

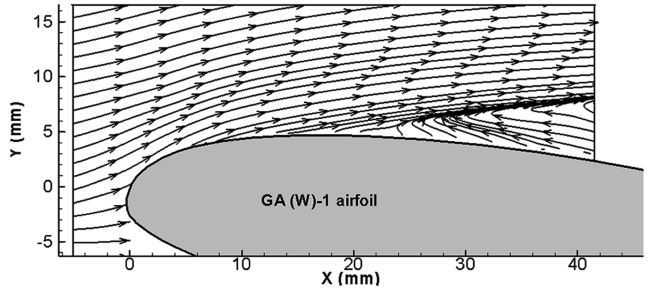

d) Streamlines of the ensemble-averaged flowfield

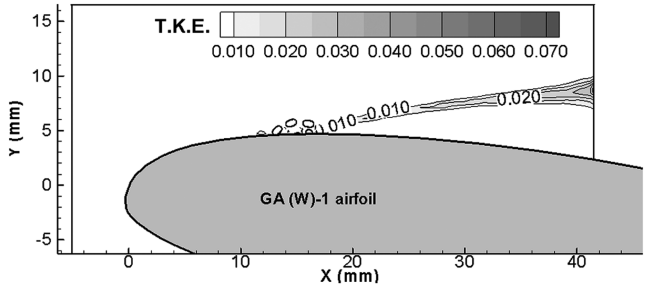

e) Normalized turbulent kinetic energy distribution

Fig. 6 Around the nose of the GA (W)-1 airfoil at AOA = 10.0 deg.

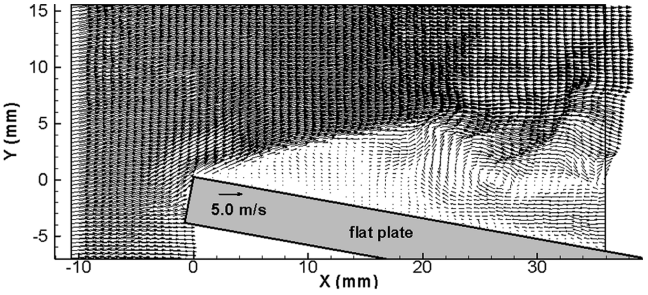

a) Instantaneous velocity field

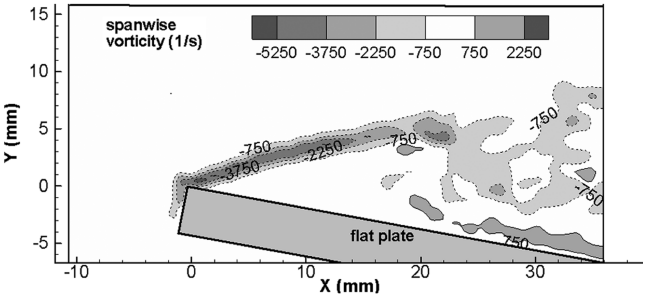

b) Instantaneous vorticity distribution

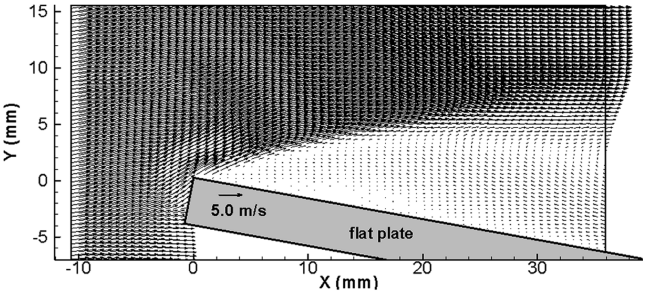

c) Ensemble-averaged velocity field

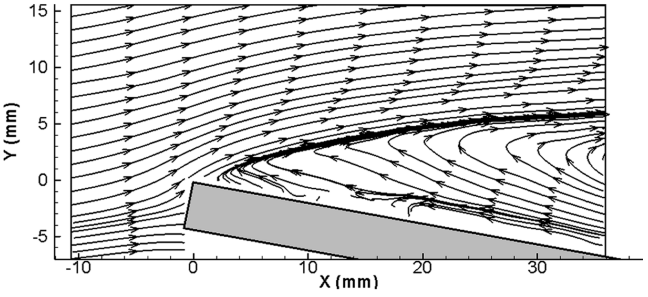

d) Streamlines of the ensemble-averaged flowfield

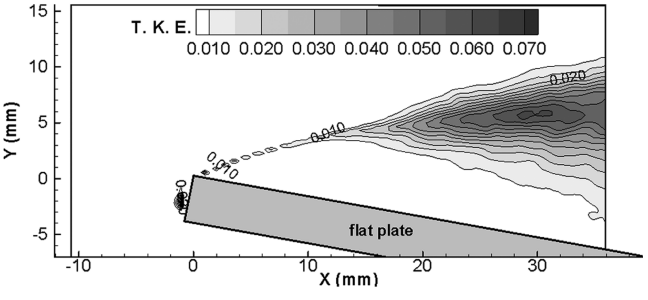

e) Normalized turbulent kinetic energy distribution

Fig. 7 Around the nose of the flat plate at AOA = 10.0 deg.

unsteady Kelvin–Helmohtz vortex structures in the flowfield when the angle of attack increases to 15.0 deg, the shedding path of the unsteady vortex structures was found to be relatively far from the surface of the corrugated airfoil. The unsteady vortex structures could no longer be trapped in the valleys of the corrugation. The ensemble-averaged velocity field and the corresponding streamlines also show clearly that the high-speed flow streams permanently separate from the upper surface of the airfoil. Although small

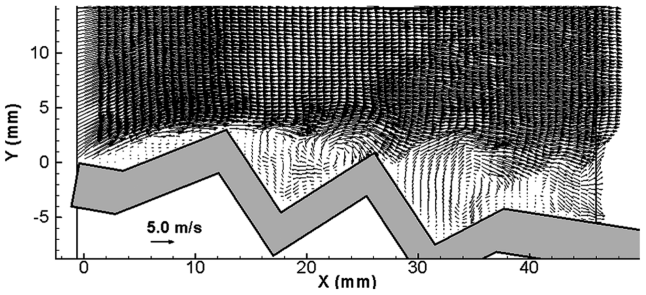

a) Instantaneous velocity field

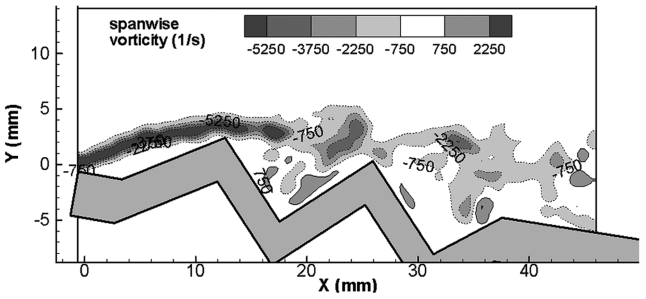

b) Instantaneous vorticity distribution

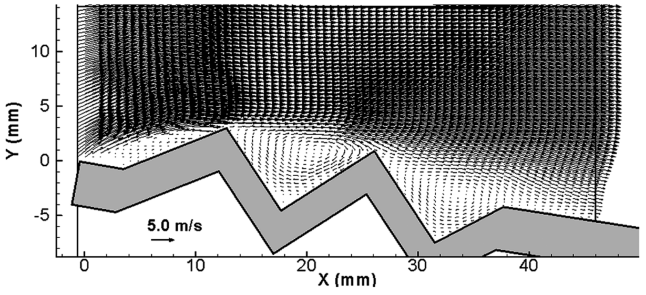

c) Ensemble-averaged velocity field

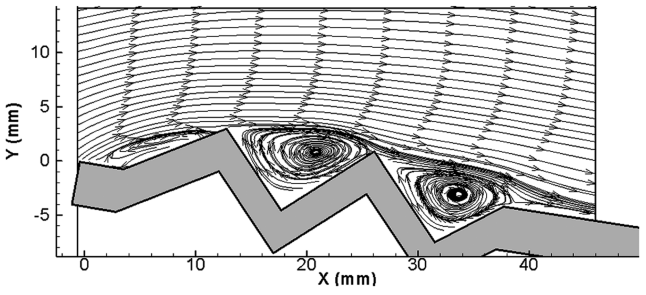

d) Streamlines of the ensemble-averaged flowfield

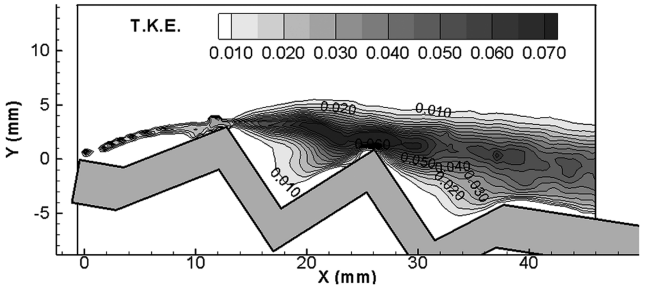

e) Normalized turbulent kinetic energy distribution

Fig. 8 Around the nose of the corrugated airfoil at AOA = 10.0 deg.

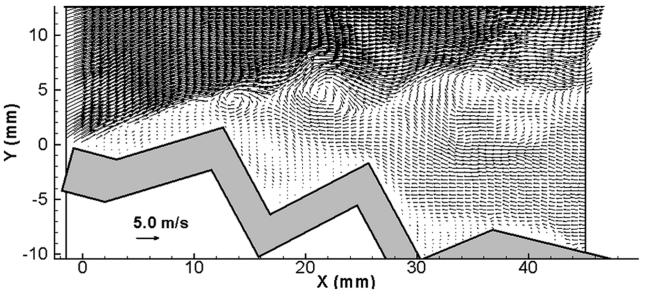

a) Instantaneous velocity field

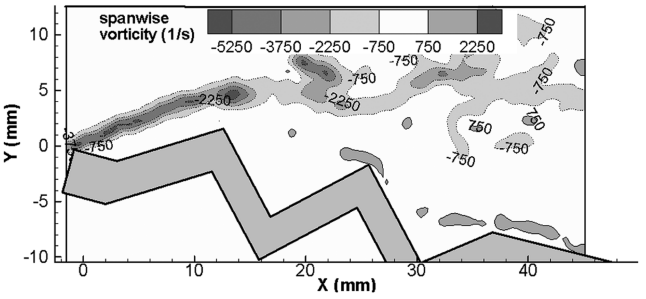

b) Instantaneous vorticity distribution

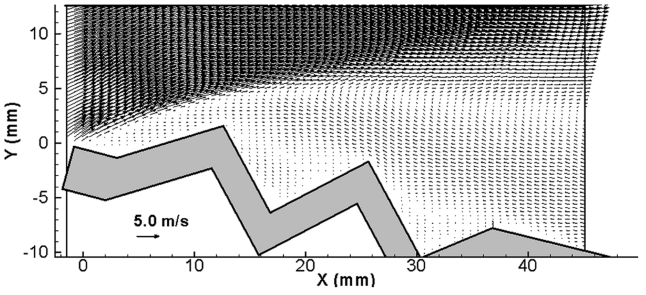

c) Ensemble-averaged velocity field

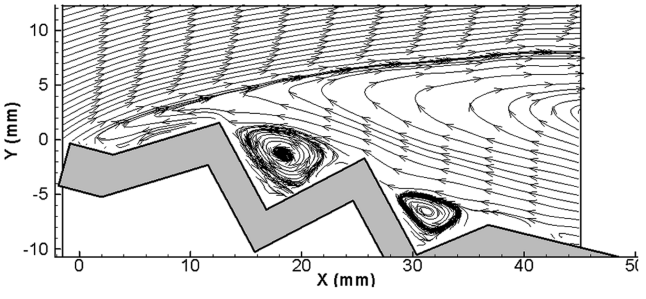

d) Streamlines of the ensemble-averaged flowfield

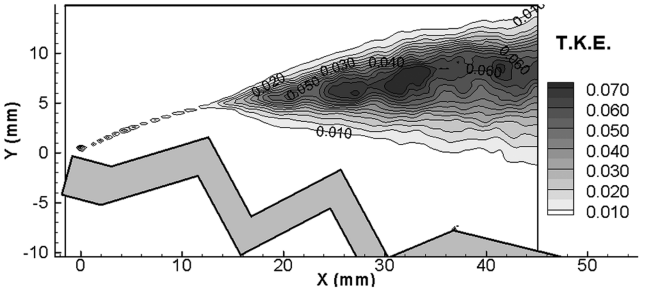

e) Normalized turbulent kinetic energy distribution

Fig. 9 Around the nose of the corrugated airfoil at AOA = 15.0 deg.

circulation bubbles were still found to sit in the valleys of the corrugated cross section, they became much weaker (i.e., much lower rotating velocity, as revealed from the velocity distributions), and their rotating direction was also found to be reversed to accommodate the reversed flow outside the valleys. The adverse pressure gradient over the upper surfaces of the airfoils would become much more significant as the angle of attack increased to 15.0 deg, which requires a much more energetic boundary layer to overcome the adverse pressure gradient over the upper surface of the airfoil. However, the measured TKE distribution reveals that the regions with higher turbulent kinetic energy were along the shedding path of the Kelvin–Helmohtz vortex structures, which is quite far from the surface of the corrugated airfoil. Therefore, large-scale flow separation and airfoil stall were found to take place on the corrugated airfoil, due to the lack of enough kinetic energy in the boundary layer to overcome the significant adverse pressure gradient, as shown in Fig. 5c.

Figure 10 shows the measured aerodynamic forces (lift and drag) acting on the test airfoils at different angles of attack. The estimated measurement uncertainties are also shown in the figure as error bars. The corrugated airfoil was found to have almost comparable lift coefficient with those of the GA (W)-1 airfoil and the flat plate when the angle of attack is relatively small (AOA < 8.0). As expected, the lift coefficient would increase almost linearly with the increasing angle of attack. As revealed in the preceding PIV measurement results, airfoil stall was found to take place at an 8.0-deg angle of attack for the flat plate. After airfoil stall, the lift coefficient profile of the flat plate was found to become almost flat, and the drag coefficient was found to increase rapidly as the angle of attack increased. Such trends of the drag-and-lift coefficient profiles for a flat plate were also reported by Kesel [12] and Sunada et al. [13]. For the GA (W)-1 airfoil, airfoil stall was found to occur at about a 9.0-deg angle of attack. As expected, the lift coefficient of the GA (W)-1 airfoil dropped significantly after airfoil stall, and the drag coefficient increased rapidly as the angle of attack increased. Because the corrugated airfoil could delay large-scale flow separation and airfoil stall up to a 12.0-deg angle of attack, the measured maximum lift coefficient for the corrugated airfoil was found to be 0.94, which is approximately 26% higher than that of the flat plate (about 0.70 at AOA $= 8.0$ deg) and 10% higher than that of the GA(W)-1 airfoil (about 0.84 at AOA $= 9.0$ deg). After airfoil stall, the lift coefficient of the corrugated airfoil was found to drop significantly, which is similar to that of the streamlined GA (W)-1 airfoil. Kesel [12] reported similar results when he measured the aerodynamic forces (lift and drag) acting on a corrugated airfoil similar to that in the present study at a lower Reynolds number of $Re = 10,000$.

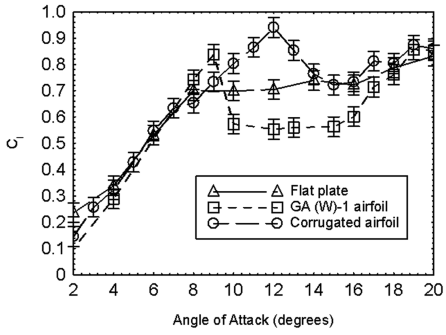

a) Measured lift coefficient

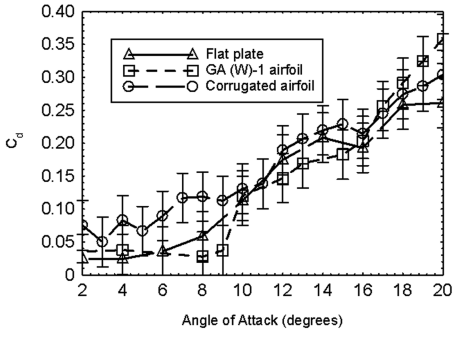

b) Measured drag coefficient

Fig. 10 Measured lift-and-drag coefficient profiles.

As shown in Fig. 10, the measured drag coefficient data were more qualitative rather than quantitative, due to the relatively poor measure accuracy at low angles of attack. The measured drag coefficient of the corrugated airfoil was found to be slightly larger than the other two airfoils when the angle of attack was relatively small (AOA < 8.0 deg). As the angle of attack became large enough (AOA > 10.0 deg), the drag coefficient of the corrugated airfoil was found to become very comparable with those of the streamlined GA (W)-1 airfoil and flat plate. This can be explained as follows: it is well known that the total drag force acting on an airfoil can be divided into friction drag and pressure drag. The friction drag is due to the shear stress acting on the surface of the airfoil. The pressure drag is due to the pressure difference around the surface of the airfoil. The pressure drag is also often referred to as the form drag, because of its strong dependence on the effective shape of the airfoil, which is usually indicated by the averaged streamline pattern around the airfoil. The pressure drag is generally much larger than the friction drag. When the angle of attack is relatively small (AOA < 8.0 deg), the slightly higher drag acting on the corrugated airfoil is believed to be closely related to the fact that the corrugated airfoil has a much larger contact area with moving flow streams (i.e., increased friction drag), due to its complex shape of the corrugated cross section. As the angle of attack becomes large enough, airfoil stall takes place for the test airfoils (i.e., flat plate at AOA $= 8.0$ deg, GA(W)-1 airfoil at AOA $= 9.0$ deg, and corrugated airfoil at AOA $= 12.0$ deg). After airfoil stall, large-scale flow separation covers the entire upper surfaces of the airfoils. The pressure drag increases dramatically, and the friction drag becomes negligible. Therefore, the drag force acting on the airfoil is mainly determined by pressure drag, which could be indicated by the streamline pattern around the airfoil. As revealed clearly in the PIV measurement results given in Fig. 5, the streamline patterns for the flow around the corrugated airfoil are very much the same as those around the GA(W)-1 airfoil and flat plate after airfoil stall; that is, a very large separation bubble would be generated to cover the entire upper surface of the airfoil. Therefore, the drag coefficient of the corrugated airfoil would become comparable with those of the GA (W)-1 airfoil and flat plate at relatively large angles of attack.

It should be noted that although the relatively big drag coefficients of the corrugated airfoil at low angles of attack may be an issue to limit their applications, especially for the MAVs flying at low angles of attack, the unique feature of the corrugated airfoil in preventing large-scale flow separations and airfoil stall can be leveraged in MAV designs to improve their flight agility and maneuverability at high angles of attack. It should also be noted that the geometric parameters of the corrugated-airfoil model used in the present study were chosen rather arbitrarily. Further systematic studies are needed to explore/optimize such bioinspired airfoil shape and wing planform design paradigms (i.e., the effects of the design parameters such as the geometry of the corrugated profile, the camber of the airfoil, the thickness of the airfoil, the stiffness of the material or flexibility of the airfoil, the corner sharpness of the corrugations, etc.) to achieve improved aerodynamic performance for MAV applications.

Conclusions

An experimental study was conducted to investigate the flow features around a bioinspired corrugated airfoil compared with a streamlined GA (W)-1 airfoil and a flat plate at a low chord Reynolds number of 34,000 to explore the potential applications of nontraditional bioinspired corrugated airfoils for MAV designs. The experimental study was conducted in a wind tunnel with particle image velocimetry to make detailed flowfield measurements in addition to total aerodynamic force measurements. The quantitative flowfield measurement results demonstrated clearly that the

corrugated airfoil could have a better performance over the streamlined airfoil and flat plate in preventing large-scale flow separation and airfoil stall at low Reynolds numbers. Because of the low Reynolds number, flow separation was found near the trailing edge of the GA (W)-1 airfoil when the angle of attack was a mere 5.0 deg, and airfoil stall was found to take place at about a 9.0-deg angle of attack for the streamlined GA (W)-1 airfoil. Large-scale flow separation was found over the entire upper surface of the flat plate as the angle of attack reached 8.0 deg. However, no apparent large-scale flow separation or airfoil stall could be found for the bioinspired corrugated airfoil up to a 12.0-deg angle of attack. The aerodynamic force (lift-and-drag) measurement results further confirmed the possibility of using such nontraditional bioinspired corrugated airfoils in MAV designs for improved agility and maneuverability.

The detailed PIV measurements elucidated the underlying physics about how and why corrugated airfoils could suppress large-scale flow separation and airfoil stall at low Reynolds numbers. It was found that the protruding corners of the corrugated airfoils would act as turbulators to generate unsteady vortex structures to promote the transition of the boundary layer from laminar to turbulent. The unsteady vortices trapped in the valleys of the corrugated cross section could pump high-speed fluid from outside to near-wall regions to provide sufficient kinetic energy within the boundary-layer flow to overcome adverse pressure gradients, thus discouraging flow separation and airfoil stall.

It should be noted that the although the bioinspired corrugated-airfoil model used in the present study has the same corrugated profile as the midsection of a dragonfly forewing, the relative thickness of the airfoil, the material stiffness, the complexity of the wing planform, the motion of the airfoil, and the working chord Reynolds number used for the present study are quite different from those of a real dragonfly. Although some of the findings derived from the present study may be useful to understand dragonfly flight aerodynamics, the flow structures revealed from the present study could be quite different from those of previous studies with free or tethered dragonflies at much lower Reynolds numbers. It is worthy of noting again that the purpose of the present study is to try to explore a nontraditional airfoil design for MAV applications through bioinspiration (i.e., by leveraging the corrugated feature of dragonfly wings), rather than to try to understand the fundamental physics of dragonfly flight aerodynamics.

Acknowledgments

The support of National Science Foundation CAREER program under award number CTS-0545918 is gratefully acknowledged.

References

[1] Mueller, T. J. (ed.), *Fixed and Flapping Wing Aerodynamics for Micro Air Vehicle Applications* Progress in Astronautics and Aeronautics, AIAA, Reston, VA, 2001.

[2] Rees, C. J. C., "Form and Function in Corrugated Insect Wings," *Nature*, Vol. 256, July 1975, pp. 200–203. doi:10.1038/256200a0

[3] Kesel, A. B., Philippi, U., and Nachtigall, W., "Biomechanical Aspects of Insect Wings–An Analysis Using the Finite Element Method," *Computers in Biology and Medicine*, Vol. 28, No. 4, 1998, pp. 423–437. doi:10.1016/S0010-4825(98)00018-3

[4] Rees, C. J. C., "Aerodynamic Properties of an Insect Wing Section and a Smooth Aerofoil Compared," *Nature*, Vol. 258, No. 13, 1975, pp. 141–142. doi:10.1038/258141a0

[5] Newman, B. G., Savage, S. B., and Schouella, D., "Model Test on a Wing Section of an Aeschna Dragonfly," *Scale Effects in Animal Locomotion*, edited by T. J. Pedley, Academic Press, London, 1977, pp. 445–477.

[6] Azuma, A., Azuma, S., Watanabe, I., and Furuta, T., "Flight Mechanics of a Dragonfly," *Journal of Experimental Biology*, Vol. 116, No. 1, 1985, pp. 79–107.

[7] Somps, C., and Luttges, M., "Dragonfly Flight: Novel Uses of Unsteady Separation Flows," *Science*, Vol. 228, No. 4705, June 1985, pp. 1326–1329. doi:10.1126/science.228.4705.1326

[8] Azuma, A., and Watanabe, T., "Flight Performance of a Dragonfly," *Journal of Experimental Biology*, Vol. 137, No. 1, 1988, pp. 221–252.

[9] Rüppell, G., "Kinematic Analysis of Symmetrical Flight Maneuvers of Odonata," *Journal of Experimental Biology*, Vol. 144, No. 1, 1989, pp. 13–42.

[10] Okamoto, M., Yasuda, K., and Azuma, A., "Aerodynamic Characteristics of the Wings and Body of a Dragonfly," *Journal of Experimental Biology*, Vol. 199, No. 2, 1996, pp. 281–294.

[11] Wakeling, J. M., and Ellington, C. P., "Dragonfly Flight 1: Gliding Flight and Steady-State Aerodynamic Forces," *Journal of Experimental Biology*, Vol. 200, No. 3, 1997, pp. 543–556.

[12] Kesel, A. B., "Aerodynamic Characteristics of Dragonfly Wing Sections Compared with Technical Aerofoil," *Journal of Experimental Biology*, Vol. 203, No. 20, 2000, pp. 3125–3135.

[13] Sunada, S., Yasuda, T., Yasuda, K., and Kawachi, K., "Comparison of Wing Characteristics at an Ultralow Reynolds Number," *Journal of Aircraft*, Vol. 39, No. 2, 2002, pp. 331–338.

[14] Thomas, A. L. R., Taylor, G. K., Srygley, R. B., Nudds, R. L., and Bomphrey, R. J., "Dragonfly Flight: Free-Flight and Tethered Flow Visualizations Reveal a Diverse Array of Unsteady Lift-Generating Mechanisms, Controlled Primarily via Angle of Attack," *Journal of Experimental Biology*, Vol. 207, No. 24, 2004, pp. 4299–4323. doi:10.1242/jeb.01262

[15] Vargas, A., and Mittal, R., "Aerodynamic Performance of Biological Airfoils," 2nd AIAA Flow Control Conference, Portland, OR, AIAA Paper 2004-2319, 2004.

[16] Luo, G., and Sun, M., "The Effects of Corrugation and Wing Planform on the Aerodynamic Force Production of Sweeping Model Insect Wings," *Acta Mechanica Sinica*, Vol. 21, No. 6, 2005, pp. 531–541. doi:10.1007/s10409-005-0072-4

[17] Kwok, M., and Mittal, R., "Experimental Investigation of the Aerodynamics of a Modeled Dragonfly Wing Section," *AIAA Region I-MA Student Conference*, AIAA, Reston, VA, 8–9 Apr. 2005, pp. 1–7.

[18] McGee, R. J., and Beasley, W. D., "Low-Speed Aerodynamics Characteristics of a 17-Percent-Thick Airfoil Section Designed for General Aviation Applications," NASA TN D-7428, 1973.

[19] Lissaman, P. B. S., "Low-Reynolds-Number Airfoils," *Annual Review of Fluid Mechanics*, Vol. 15, 1983, pp. 223–239. doi:10.1146/annurev.fl.15.010183.001255

[20] Gad-el-Hak, M., "Micro-Air-Vehicles: Can They Be Controlled Better," *Journal of Aircraft*, Vol. 38, No. 3, 2001, pp. 419–429.